remote sensing

MDPI

Article

A Spatial Reconstruction Method of Ionospheric foF2 Based on High Accuracy Surface Modeling Theory

Jian Wang [1,2,3], Han Han [1] and Yafei Shi [1,2,*]

[1] School of Microelectronics, Tianjin University, Tianjin 300072, China; wangjian16@tju.edu.cn (J.W.)
[2] Qingdao Institute for Ocean Technology, Tianjin University, Qingdao 266200, China
[3] Key Laboratory of Organic Integrated Circuit, Ministry of Education, Tianjin University, Tianjin 300072, China
* Correspondence: shiyafei@tju.edu.cn

Abstract: The ionospheric F2 critical frequency (foF2) is one of the most crucial application parameters in high-frequency communication, detection, and electronic warfare. To improve the accuracy of spatial reconstruction of the ionospheric foF2, we propose a high-accuracy surface (HAS) modeling method. This method converts difficult-to-solve differential equations into more manageable algebraic equations using direct difference approximation, significantly reducing algorithm complexity and computational load while exhibiting excellent convergence properties. We used seven stations in Brisbane, Canberra, Darwin, Hobart, Learmonth, Perth, and Townsville, with one station as a validation station and six as training stations (e.g., Brisbane as a validation station and the other stations—Canberra, Darwin, Hobart, Learmonth, Perth, and Townsville—as training stations). The training stations and the HAS method were used to train and reconstruct the validation stations at different solar activity periods, seasons, and local times. The predicted values of the validation stations were compared with the measured values, and the proposed method was analyzed and validated. The reconstruction results show the following. (1) The relative root mean square errors (RRMSEs) of HAS method prediction in different solar activity epochs were 13.67%, 7.74%, and 9.19%, respectively, which are 13.57%, 7.41%, and 6.41% higher than the prediction accuracy of the Kriging method, respectively. (2) In the four seasons, the RRMSEs of the HAS method prediction are 9.27%, 13.1%, 8.81%, and 8.09%, respectively, which are 10.83%, 11.73%, 4.25%, and 12.00% higher than the prediction accuracy of the Kriging method. (c) During the daytime and nighttime, the RRMSEs of HAS method prediction were 9.23% and 11.17%, which were 5.92% and 11.99% higher than the prediction accuracy of the Kriging method, respectively. (d) Under the validation dataset, the average predictive RRMSE of the HAS method was 10.29%, and the average predictive RRMSE of the IRI prediction model was 12.35%, with a 2.06% improvement in the predictive accuracy of the HAS method. In general, the prediction effect of the HAS method was better than that of the Kriging method, thus verifying the effectiveness and reliability of the proposed method. In summary, the proposed reconstruction method is of great significance for improving usable frequency prediction and enhancing communication performance.

Keywords: HAS; foF2; ionosphere; spatial reconstruction

check for updates

Citation: Wang, J.; Han, H.; Shi, Y. A Spatial Reconstruction Method of Ionospheric foF2 Based on High Accuracy Surface Modeling Theory. *Remote Sens.* **2024**, *16*, 3247. https://doi.org/10.3390/rs16173247

Academic Editors: Chunhua Jiang, Huijun Le, Ercha Aa and Zheng Li

Received: 25 July 2024
Revised: 27 August 2024
Accepted: 31 August 2024
Published: 2 September 2024

1. Introduction

The ionosphere is a crucial component of the Sun-Earth space environment, affecting the performance of various radio information systems such as satellite navigation, communication, and radar due to its refraction, reflection, scattering, and absorption effects on radio waves passing through it. Therefore, studying the ionosphere's characteristic parameters and understanding its spatiotemporal variations are of significant practical value for high-frequency communications, terrestrial and space radio links, and other applications [1]. The ionosphere, characterized by complex and variable plasma activities, functions as a nonlinear system with random temporal and spatial fluctuations. Notably, the F2 layer within the ionosphere harbors the highest electron concentration, significantly influencing different radio propagation modes [2]. The critical frequency of the F2 layer (foF2) is a key parameter for ionospheric research and a primary focus for studying ionospheric plasma disturbances. In addition, foF2 is extensively utilized in space weather [3] and high-frequency communications [4], among other applications. Accurate forecasting of the foF2 is crucial for these applications. The foF2 varies with diurnal and seasonal cycles and solar activity, and it is strongly correlated with spatial latitude and longitude [5]. Accurate reconstruction of the foF2 is thus critical for understanding and utilizing the ionosphere [6]. The foF2 can be directly or indirectly observed by vertical and oblique ionospheric detectors [7]. If no ionospheric detection station exists, then these parameters can be obtained by reconstructing the spatial reconstruction model.

For a long time, ionospheric reconstruction has been a major focus of ionospheric research. Scholars worldwide have continuously studied ionospheric regional reconstruction technology to improve the accuracy of ionospheric parameter predictions. In recent years, researchers have gradually established models in localized regions such as China [8], Europe [9], and Oceania [10]. Typical examples include inverse distance weighted interpolation [11], thin-plate spline interpolation [12], spherical harmonics [13,14], and Kriging interpolation [15]. These methods have demonstrated good performance in reflecting the global or local spatial distribution characteristics of the foF2. On one hand, based on the coverage of models, foF2 spatial reconstruction can be divided into global and regional types. Models like IRI [16] and ITU-R [17] span large spatial scales, offering more generalized predictions by considering the overall features of the global ionosphere and focusing on large-scale spatial structures. On the other hand, regional models, which require higher real-time performance, can accurately predict small- and medium-scale changes in the foF2 within localized areas. Therefore, regional models are mainstream in current research and are essential for future communication system applications [18].

To enhance the accuracy of spatial reconstruction of the ionospheric foF2, we adopted the HAS modeling theory. This method typically produces optimal results in spatial data interpolation [19]. One key advantage is that the coefficient matrix of the linear algebraic equations remains constant in each iteration [20], necessitating only a single inverse calculation, which significantly lowers the computational burden [21]. After years of iteration, the HAS method has achieved excellent results in many fields [22,23]. This paper is structured as follows. First, we introduce the background and significance of ionospheric research and foF2 parameter studies. Second, we sequentially introduce the data, concepts, methods, and specific modeling processes used. Then, we compare the proposed model with IRI and Kriging to verify the method's correctness and effectiveness. Finally, we summarize the effects of reconstruction of the ionospheric foF2 parameter.

2. Data and Methods

2.1. Data Collections

The data used in this study came from the Global Ionospheric Radio Observatory (GIRO), which provides public access to ionospheric observations collected at multiple locations and has real-time feeds available for most stations, offering precise and detailed information on ionospheric observations [24]. The spatial reconstruction range in this study was 110°–160°E longitude and 10°–45°S latitude, with a spatial resolution of 0.5° × 0.5°, collecting data from seven stations from 2013 to 2018. The seven stations' latitudes, longitudes, and distributions are shown in Figure 1.

In the spatial reconstruction of the ionospheric foF2, to ensure the same sampling interval for the foF2 across different stations, a fixed sampling interval of 60 min was selected. The data collection periods for the seven stations at Brisbane, Canberra, Darwin, Hobart, Learmonth, Perth, and Townsville involved 1584, 1570, 1583, 1560, 952, 1560, and 1466 data points, respectively, from 2013 to 2018. Next the following procedures were carried out:

1. The raw GIRO dataset includes 24 h of data collected daily. Initially, we computed the monthly average of the data at the seven stations and stored them sequentially. Missing data between 2013 and 2018 at the seven stations were supplemented with foF2 data predicted by the International Reference Ionosphere (IRI) model to facilitate spatial reconstruction.
2. Given that the resolution of the data used for HAS modeling was 5° × 5°, we approximated the latitude and longitude of each station to the closest whole number and stored the monthly average foF2 values at fixed times in corresponding grid points to facilitate interpolation.

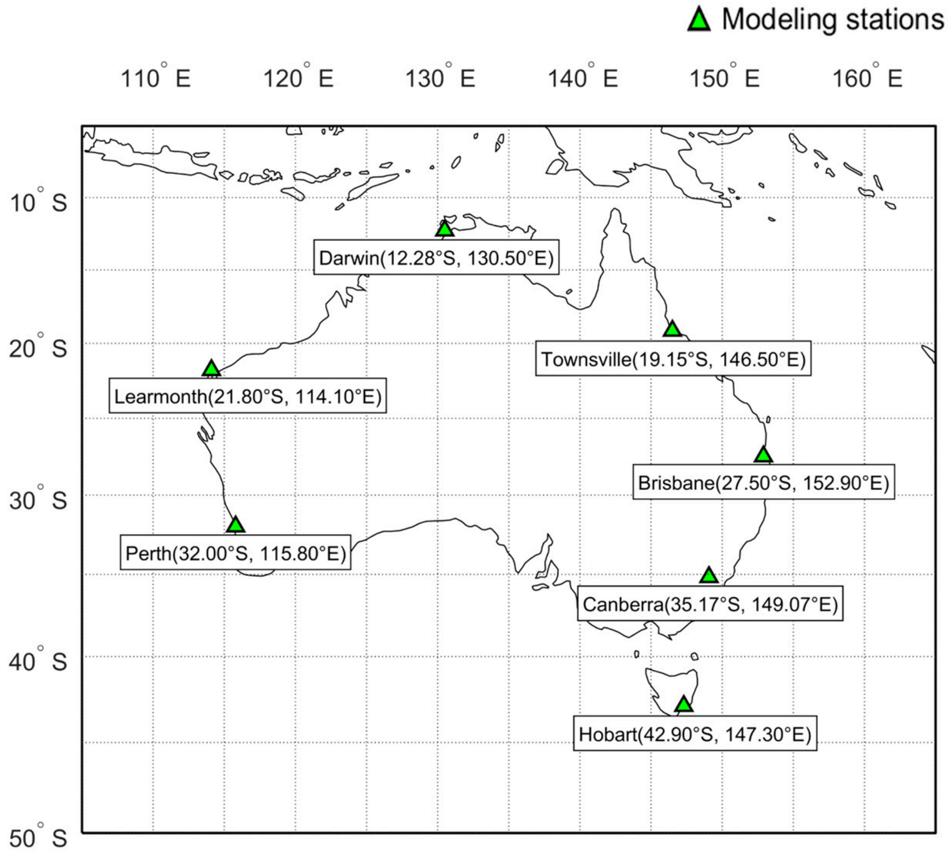

Figure 1. The spatial distribution of seven modeling stations within Oceania. These stations included Brisbane, Canberra, Darwin, Hobart, Learmonth, Perth, and Townsville.

2.2. Modeling Data

The spatial modeling process of this study is shown in Figure 2. The first step was to generate a 5° × 5° grid within the model coverage range (110°E–160°E longitude and 10°–45°S latitude) and fill in this grid with the IRI model's predicted data values. The second step was to put the actual observed foF2 values from the training stations into the corresponding adjacent grid to obtain the observed surface. The third step involved using the high-accuracy surface (HAS) modeling method to iteratively refine the observed surface to further improve the model's accuracy. The fourth step used Kriging interpolation to interpolate the 5 × 5 iterative surface of the completed HAS model to generate a 0.5° × 0.5° grid. Finally, cross-validation was used to verify and analyze the model's accuracy by selecting six out of the seven modeling stations as training stations and the remaining one as the validation station, followed by comparing the accuracy of the model when using the IRI model and Kriging interpolation to confirm the correctness and effectiveness of the proposed method.

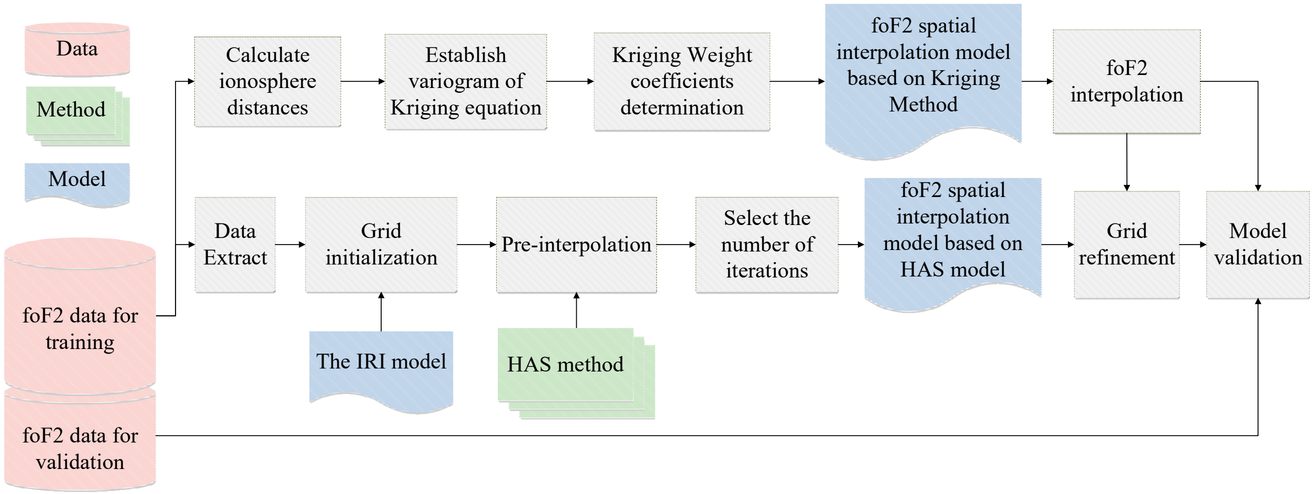

Figure 2. Modeling flowchart of foF2 spatial interpolation model based on Kriging model and foF2 spatial interpolation model based on Kriging model.

To test the impact of the two models on reconstruction accuracy, this study used the RRMSE as the standard for method evaluation:

$$\delta = \sqrt{\frac{1}{Y}\sum_{y=1}^{Y}\left(\frac{f_{\text{obs}}^{y} - f_{\text{mod}}^{y}}{f_{\text{obs}}^{y}}\right)^{2}} \times 100\% \tag{1}$$

where δ is the RRMSE, Y is the number of cross-validations, f_{obs}^{y} is the actual observed foF2 value at the validation station, and f_{mod}^{y} is the reconstructed predicted foF2 value at the validation station for the yth iteration.

2.3. Modeling Methods

This paper integrates HAS modeling with the characteristics of the ionospheric foF2 to perform spatial reconstruction. The initial surface function of the foF2 spans the modeling range and incorporates the IRI as the background field, being expressed as follows:

$$f\text{oF2} = f(\varphi, \lambda) \tag{2}$$

where f is the mapping satisfied by the surface, φ represents the longitude of the ionospheric observation station, λ represents the latitude of the ionospheric observation station, and (φ,λ) represents the coordinates of the ionospheric observation station.

During the numerical simulation of the function, the first and second fundamental quantities of the surface must first be interpolated using the sampled values [25]. According to the fundamental theorem of surfaces, the first and second fundamental quantities define many surface properties. The first fundamental quantities represent geometric properties, such as the length of the curves and the area of the surfaces [26]. In contrast, the second fundamental quantity represents macro information on the surface, such as local warping [27]. The first fundamental quantities B, C, and D can be expressed as follows:

$$\begin{cases} B = 1 + f_{\varphi}^{2} \\ C = f_{\varphi} f_{\lambda} \\ D = 1 + f_{\lambda}^{2} \end{cases} \tag{3}$$

where f_φ and f_λ are denoted as the first-order derivatives of the function f(φ,λ) in the φ and λ directions, respectively.

The second class of fundamental quantities E and F is denoted as

$$\begin{cases} E = \frac{f_{\varphi\varphi}}{\sqrt{1+f_{\varphi}^2+f_{\lambda}^2}} \\ F = \frac{f_{\lambda\lambda}}{\sqrt{1+f_{\varphi}^2+f_{\lambda}^2}} \end{cases} \tag{4}$$

where $f_{\varphi\varphi}$ and $f_{\lambda\lambda}$ are the second-order derivatives of the function f(φ,λ) in the φ and λ directions, respectively. Based on surface theory and space sampling, the surface can be expressed by the following set of Gaussian equations:

$$\begin{cases} f_{\varphi\varphi} = G_{11}^1 f_{\varphi} + G_{11}^2 f_{\lambda} + \frac{E}{\sqrt{B+D-1}} \\ f_{\lambda\lambda} = G_{22}^1 f_{\varphi} + G_{22}^2 f_{\lambda} + \frac{F}{\sqrt{B+D-1}} \end{cases} \tag{5}$$

where G_{11}^1, G_{11}^2, G_{22}^1, and G_{22}^2 are the coefficients of the Gaussian system of equations and depend only on the fundamental quantities of the first type and their derivatives, defined as

$$\begin{cases} G_{11}^1 = \frac{DB_{\varphi}-2CC_{\varphi}+CB_{\lambda}}{2(BD-C^2)} \\ G_{22}^1 = \frac{2DC_{\lambda}-DD_{\varphi}-CD_{\lambda}}{2(BD-C^2)} \\ G_{11}^2 = \frac{2BC_{\varphi}-BB_{\lambda}-CB_{\varphi}}{2(BD-C^2)} \\ G_{22}^2 = \frac{BD_{\lambda}-2CC_{\lambda}+CD_{\varphi}}{2(BD-C^2)} \end{cases} \tag{6}$$

The results of the numerical experimental analyses show that the inverse of the coefficient matrix needs to be reinverted at each iteration, which is highly computationally intensive.

To reduce the computational effort, the finite difference form's expression of the Gaussian system of equations is updated as follows [28]:

$$\begin{cases} \frac{f_{i+1,j}^{n+1}-2f_{i,j}^{n+1}+f_{i-1,j}^{n+1}}{{h_{\varphi}}^2} = (G_{11}^1)_{i,j}^n \frac{f_{i+1,j}^n-f_{i-1,j}^n}{2h_{\varphi}} + (G_{11}^2)_{i,j}^n \frac{f_{i,j+1}^n-f_{i,j-1}^n}{2h_{\lambda}} + \frac{E_{i,j}^n}{\sqrt{B_{i,j}^n+D_{i,j}^n-1}} \\ \frac{f_{i,j+1}^{n+1}-2f_{i,j}^{n+1}+f_{i,j-1}^{n+1}}{{h_{\lambda}}^2} = (G_{22}^1)_{i,j}^n \frac{f_{i+1,j}^n-f_{i-1,j}^n}{2h_{\lambda}} + (G_{22}^2)_{i,j}^n \frac{f_{i,j+1}^n-f_{i,j-1}^n}{2h_{\lambda}} + \frac{F_{i,j}^n}{\sqrt{B_{i,j}^n+D_{i,j}^n-1}} \end{cases} \tag{7}$$

where n denotes the number of iterations. From Equation (7), it can be found that the left-hand side's coefficient matrices of the solved system of linear algebraic equations are the same in each iteration such that the inverse matrices are required only once, thus reducing the computational effort considerably.

In this case, the finite difference form of the fundamental quantities of the first category and the second category is shown below:

$$\begin{cases} B_{i,j} = 1 + (\frac{\widetilde{f}_{i+1,j}-\widetilde{f}_{i-1,j}}{2h_{\varphi}})^2 \\ C_{i,j} = (\frac{\widetilde{f}_{i+1,j}-\widetilde{f}_{i-1,j}}{2h_{\varphi}})(\frac{\widetilde{f}_{i,j+1}-\widetilde{f}_{i,j-1}}{2h_{\lambda}}) \\ D_{i,j} = 1 + (\frac{\widetilde{f}_{i,j+1}-\widetilde{f}_{i,j-1}}{2h_{\lambda}})^2 \end{cases} \tag{8}$$

$$\left\{\begin{array}{l} E_{i,j}=\dfrac{\frac{\widetilde{f}_{i+1,j}-2\widetilde{f}_{i,j}+\widetilde{f}_{i-1,j}}{h_{\varphi}^{2}}}{\sqrt{1+(\frac{\widetilde{f}_{i+1,j}-\widetilde{f}_{i-1,j}}{2h_{\varphi}})^{2}+(\frac{\widetilde{f}_{i,j+1}-\widetilde{f}_{i,j-1}}{2h_{\lambda}})^{2}}} \\ F_{i,j}=\dfrac{\frac{\widetilde{f}_{i,j+1}-2\widetilde{f}_{i,j}+\widetilde{f}_{i,j-1}}{h_{\lambda}^{2}}}{\sqrt{1+(\frac{\widetilde{f}_{i+1,j}-\widetilde{f}_{i-1,j}}{2h_{\varphi}})^{2}+(\frac{\widetilde{f}_{i,j+1}-\widetilde{f}_{i,j-1}}{2h_{\lambda}})^{2}}} \end{array}\right. \tag{9}$$

where h_{φ} and h_{λ} are the calculation steps in the longitude and latitude directions and $\widetilde{f_{i,j}}$ is the predicted value of the foF2 calculated by the IRI model at the grid position (φ_i,λ_j).

The finite difference formulation of the Gaussian system of equations with coefficients G_{11}^{1}, G_{11}^{2}, G_{22}^{1}, and G_{22}^{2} are

$$\left\{\begin{array}{l} (G_{11}^{1})_{i,j}=\dfrac{D_{i,j}(B_{i+1,j}-B_{i-1,j})h_{\lambda}-2C_{i,j}(C_{i+1,j}-C_{i-1,j})h_{\lambda}+C_{i,j}(B_{i,j+1}-B_{i,j-1})h_{\varphi}}{4(B_{i,j}D_{i,j}-C_{i,j}^{2})h_{\varphi}h_{\lambda}} \\ (G_{22}^{1})_{i,j}=\dfrac{2D_{i,j}(C_{i,j+1}-C_{i,j-1})h_{\varphi}-D_{i,j}(D_{i+1,j}-D_{i-1,j})h_{\lambda}+C_{i,j}(D_{i,j+1}-D_{i,j-1})h_{\varphi}}{4(B_{i,j}D_{i,j}-C_{i,j}^{2})h_{\varphi}h_{\lambda}} \\ (G_{11}^{2})_{i,j}=\dfrac{2B_{i,j}(C_{i+1,j}-C_{i-1,j})h_{\lambda}-B_{i,j}(B_{i,j+1}-B_{i,j-1})h_{\varphi}+C_{i,j}(B_{i,j+1}-B_{i,j-1})h_{\varphi}}{4(B_{i,j}D_{i,j}-C_{i,j}^{2})d_{\varphi}d_{\lambda}} \\ (G_{22}^{2})_{i,j}=\dfrac{B_{i,j}(D_{i,j+1}-D_{i,j-1})h_{\varphi}-2C_{i,j}(C_{i,j+1}-C_{i,j-1})h_{\varphi}+C_{i,j}(D_{i+1,j}-D_{i-1,j})h_{\lambda}}{4(B_{i,j}D_{i,j}-C_{i,j}^{2})h_{\varphi}h_{\lambda}} \end{array}\right. \tag{10}$$

The difference steps in the longitude and latitude directions are expressed as follows:

$$\left\{\begin{array}{l} h_{\varphi}=\frac{1}{\varphi+1} \\ h_{\lambda}=\frac{1}{\lambda+1} \end{array}\right. \tag{11}$$

where φ denotes the number of grid points along the longitude direction and λ represents the number of grid points along the latitude direction. The algebraic equations are then reformulated into matrix form. The matrix expression's form of the numerical simulation equations for the HAS method is

$$\left\{\begin{array}{l} Lf^{n+1}=M^{n} \\ Jf^{n+1}=N^{n} \end{array}\right. \tag{12}$$

where $f^{n+1}=[f_{1,1}^{n+1},\ldots f_{1,\lambda}^{n+1},f_{2,1}^{n+1},\ldots f_{2,\lambda}^{n+1},\ldots f_{\varphi-1,1}^{n+1},\ldots f_{\varphi-1,\lambda}^{n+1},f_{\varphi,1}^{n+1},\ldots f_{\varphi,\lambda}^{n+1}]$, T_0 is the interpolation result of the sampling point value, L and Mn are the left end's coefficient matrix and the right end's constant term matrix of the first equation in the HAS equation system, respectively, and J and N^n are the left end's coefficient matrix and the right end's constant term matrix of the second equation in the HAS equation system, respectively.

As explained in the HAS principle, the coefficient matrices located at the left end of the Gaussian equation system are presented in Figure 3, and it is evident that both L and J were fixed only at specific points, with the remaining values set to zero. Thus, the iterative process requires computation of the coefficient matrices' inverses just once [29], and the computation time of the HAS method did not significantly increase with the number of iterations.

Let $H = [L, J]^T$ and $K^n = [M^n, N^n]^T$. To ensure that the simulated values at the training stations consistently matched the actual observed values, the least squares problem was formulated with the following equation constraints:

$$\left\{\begin{array}{l} \min\left|\left|HF^{n+1}-K^{n}\right|\right|_{2} \\ s.t.\ PF^{n+1}=Q \end{array}\right. \tag{13}$$

where P is the sampling matrix, P(k, (n − 1) × λ + j) = 1, Q(m) = $\widetilde{f_{i,j}}$, and the foF2 value at the kth training station is ensured to be derived from an actual observation.

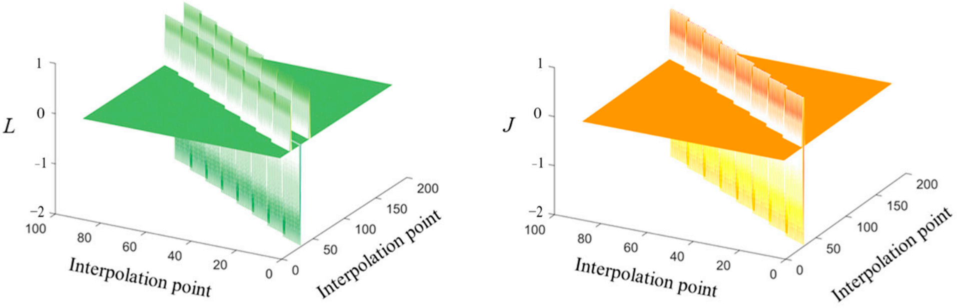

(a) (b)

Figure 3. Gaussian equations for the left side of the coefficient matrix: (**a**) L (Green color) and (**b**) J (Orange color). Both L and J were fixed only at specific points, with the remaining values set to zero.

For sufficiently large η, the HAS method can be transformed for solving the unconstrained least squares problem:

$$\min\left\|\begin{bmatrix} H \\ \eta P \end{bmatrix} F^{n+1} - \begin{bmatrix} K^{n} \\ \eta Q \end{bmatrix}\right\|_2 \tag{14}$$

In other words, it solves

$$[H^{\mathrm{T}}\ \eta P^{\mathrm{T}}]\begin{bmatrix} H \\ \eta P \end{bmatrix} F^{n+1} = [K^{\mathrm{T}}\ \eta Q^{\mathrm{T}}]\begin{bmatrix} K \\ \eta Q \end{bmatrix} \tag{15}$$

Subsequently, the issue is ultimately converted into solving a set of linear algebraic equations:

$$AF^{n+1} = R^{n} \tag{16}$$

or

$$F^{n+1} = A^{-1}R^{n} \tag{17}$$

In summary, the process of applying the HAS method to achieve surface reconstruction in foF2 space is as follows:

1. Generate a grid covering the modeling range, complete the data on the grid using the foF2 predicted by the IRI model, and then fill in the corresponding grid with the actual foF2 observations at the training station to generate the foF2's initial value surface.
2. Normalize the foF2's initial value surface and compute the surface's first class of fundamental quantities B, C, and D, second class of fundamental quantities E and F, and the Gaussian system of equations with the coefficients G^1_{11}, G^2_{11}, G^1_{22}, and G^2_{22}.
3. For n ≥ 0, solve the iterative equations $Lf^{n+1} = M^{n}$ and $Jf^{n+1} = N^{n}$ for the latitudinal and longitudinal directions, respectively.
4. For n ≥ 0, perform appropriate iterations to solve the iterative equation $AF^{n+1} = R$ and obtain the numerical solution of the surface under the given boundary conditions. Then, apply inverse normalization to derive the predicted foF2 value at the validation station.

3. Results

To show the effect of the HAS method comprehensively, Figure 4 illustrates the change in the predicted RRMSE of the HAS method with the number of iterations at seven modeling stations during various randomly chosen times. As shown in Figure 4, the predicted RRMSE of the HAS model progressively diminished and exhibited a convergence trend as the iterations increased. The convergence rates differed across the stations, and the final prediction errors were also significantly different, with some stations achieving better results with more than 30 iterations and others requiring more than 40 iterations to achieve better results.

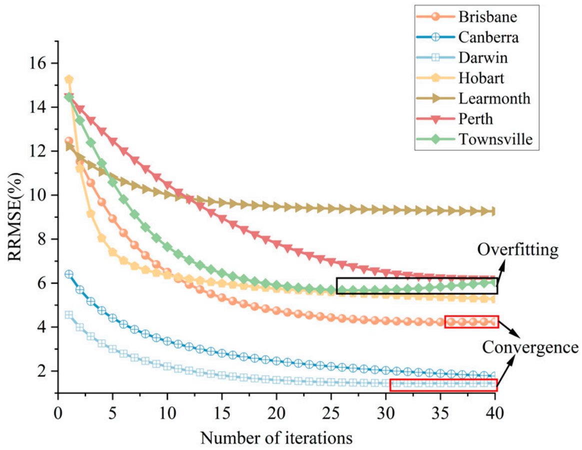

Figure 4. The HAS model's predicted RRMSEs of seven modeling stations at different times changed with the number of iterations. Convergence, overfitting, and non-convergence were observed.

The choice of the number of iterations is crucial in the HAS regional foF2 spatial reconstruction method. To ensure the accuracy of the model and avoid overfitting, we adopted the following strategies:

1. Based on experience and experimental results, we set the maximum number of iterations to 40. This setting was based on the observed model convergence and performance in multiple experiments.
2. During the iteration process, we continuously observed the model's performance, tracking the trend of the RRMSE at the validation station in particular. The judgment criteria for overfitting were mainly based on the results of cross-validation. When the RRMSE of the validation station showed a significant upward trend in several consecutive iterations, we considered that the model may have started to overfit and stopped the iteration immediately.

1. The Darwin station has the best prediction effect, converging at iteration 31 with an RRMSE of 1.44%. The Learmonth station had a worse prediction effect, with an RRMSE of 9.26% at iteration 40, mainly because Learmonth had a higher amount of missing data during the modeling time, which had a certain negative impact on the effect of the iteration.
2. The Brisbane station had a better convergence effect, and a stable prediction error was obtained at 35 iterations. The Perth station reached convergence at iteration 38, with an RRMSE of 6.20%. The Canberra, Hobart, and Learmonth stations reached a better prediction effect after 40 iterations, but their errors still showed a decreasing trend.
3. The Townsville station achieved better prediction at the 26th iteration, but after continuing the iteration, the prediction error showed a slight increase in the trend of overfitting. Therefore, applying the HAS method requires proper selection of the number of iterations to obtain a smaller error rate.
4. Taken together, the average RRMSE of 40 iterations for the seven stations above at different times was 4.83%, which demonstrates the accuracy and efficacy of the HAS method. Additionally, we employed the same approach to ascertain the necessary number of HAS iterations required to achieve the foF2 prediction using the HAS method, and the prediction results all converged to a satisfactory accuracy.

4. Discussion

As shown in Figure 5, we first divided the solar activity epochs into three periods: a high year, moderate year, and low year. Then, the foF2 data for the four seasons of spring, summer, autumn, and winter were selected. Next, the foF2 data were further divided into daytime and nighttime categories. The final composition was assigned to different validation datasets to ensure the coverage of different solar activity levels, seasons, and periods, thus ensuring the comprehensiveness and representativeness of the validation.

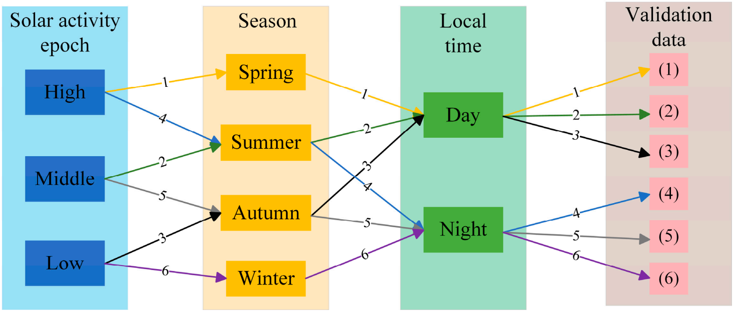

Figure 5. Validation data were divided based on solar activity epochs, seasons, and local time.

To provide a clearer explanation of the statistical variations in the HAS method's foF2 predictions, relatively high, moderate, and low solar activity periods were classified based on the monthly average sunspot number as shown in Figure 6a, where a sunspot number greater than 100 is a period of high solar activity, a sunspot number in the range of [10, 100] is a period of moderate solar activity, and a sunspot number less than 10 is a period of low solar activity [30].

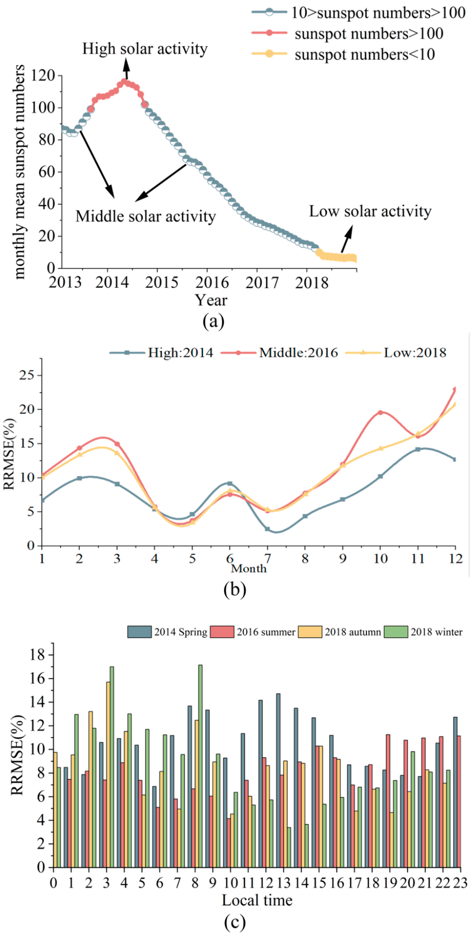

Figure 6. Solar activity epochs, seasons, and their corresponding predicted RRMSEs. (**a**) Monthly mean sunspot numbers. (**b**) Predicted RRMSEs for different solar activity epochs. (**c**) Predicted RRMSEs for different seasons.

Figure 6a shows the variation in the monthly mean of sunspot numbers during 2013–2018, with the high solar activity period mainly concentrated in 2014, the medium solar activity period was mainly distributed in 2013 and 2015–2017, and the low solar activity period was mainly concentrated in 2018. Figure 6b demonstrates the predicted RRMSEs for different solar activity periods. In different solar activity periods, the RRMSEs which were poorly predicted were higher in spring and summer, and the RRMSEs which were more accurately predicted were lower in winter. As a whole, the high solar activity periods predicted the foF2 better than the other solar activity periods, and the prediction was better in winter. The predicted RRMSEs for different seasons can be seen in Figure 6c. Specifically, the RRMSEs for spring 2014 and winter 2018 were relatively high at most time points, indicating relatively large prediction errors. The RRMSEs for summer 2016 and autumn 2018 were usually relatively low, indicating relatively good predictions. Figure 6 shows the distribution of RRMSEs under different solar activity periods and seasons, which provides an important basis for analyzing the foF2 prediction model.

4.1. Comparison between the IRI Model and HAS Method

The IRI prediction model has a wide range of spatial scales and can provide better average age prediction according to the change in characteristics of the global ionospheric surface domain. In addition, in the reconstruction process of the HAS method, because the actual data of the stations were sometimes missing, they could not be reconstructed, and the IRI prediction model was used to supplement the missing data. Therefore, the HAS model was first compared with the predicted RRMSEs of the IRI model. Figure 7 compares the results of the IRI model based on the validation data and the HAS method. The results show that the average RRMSE of IRI prediction was larger, and the prediction accuracy of the HAS method improved by 2.06%, which verifies the effectiveness of the HAS method.

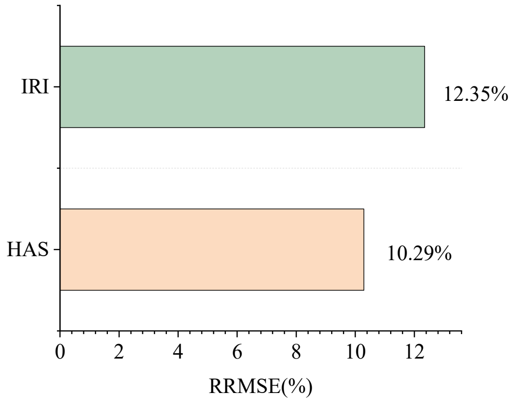

Figure 7. Comparison of the results of the two predictions of the IRI model and the HAS method.

4.2. Comparison between the Kriging Method and HAS Method

In addition to our comparison with the IRI prediction model initially used in the modeling process, we also considered a comparison with the now most-used Kriging interpolation method. Kriging interpolation is widely utilized for reconstructing regional ionospheric parameters like the foF2 and is known for proving high-quality reconstructions [31]. The Kriging method was chosen for comparison with the HAS method. The step of using the enhanced Kriging method for foF2 interpolation is outlined below. Firstly, we used the variational function established by the Euclidean distance between the observation station points and found the spatial relativity. Secondly, we used the optimal linear unbiased estimation as the foundation and the minimum estimation variance as the standard to solve for the weight coefficients of each training station relative to the validation station. We ensured that the sum of these weight coefficients was equal to one. According to the weight coefficients, the actual observations of the training stations were used to achieve the foF2 reconstruction results of the validation stations. Next, six out of the seven modeling stations were sequentially designated as training stations, while the remaining one served as the validation station. The foF2 predictions for the validation station were then computed using both the Kriging method and the HAS method. The RRMSEs of the seven stations were calculated as the final prediction RRMSE of the six validation datasets mentioned above, and the results shown in Table 1 were obtained.

Table 1. Validation dataset prediction results based on solar activity epochs, seasons, and local time.

No.	Solar Activity Epoch	Year	Season	Month	Local Time			RRMSE (%)		Increase (%)
					Time	Day	Night	Kriging	HAS	
(1)	High	2014	Spring	November	10:00	Yes		20.10	9.27	10.83
(2)	Middle	2016	Summer	January	12:00	Yes		15.28	8.13	7.15
(3)	Low	2018	Autumn	March	15:00	Yes		11.11	10.28	0.83
(4)	High	2014	Summer	December	03:00		Yes	34.37	18.07	16.30
(5)	Middle	2017	Autumn	April	22:00		Yes	15.01	7.34	7.67
(6)	Low	2018	Winter	July	21:00		Yes	20.09	8.09	12.00
Mean								19.33	10.20	9.13

As shown in Figure 8, it can be seen that the predictions of the HAS method were significantly better than those of the Kriging interpolation method.

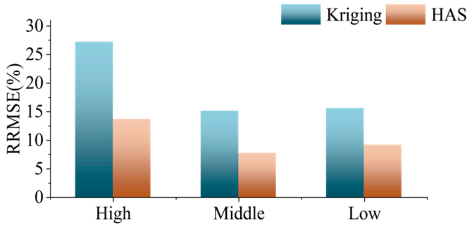

(a) Solar activity epochs

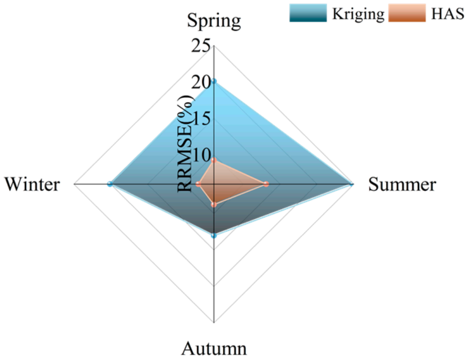

(b) Seasom

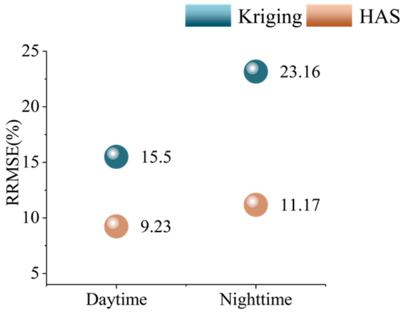

(c) Local time

Figure 8. Comparison of the results of the two predictions of the Kriging and HAS methods. (**a**) Solar activity epochs. (**b**) Season. (**c**) Local time.

1. The RRMSEs at different solar activity levels are given in Figure 8a. The Kriging and HAS methods obtained the optimal forecasting outcomes with prediction RRMSEs of 15.15% and 7.74%, respectively, during the middle solar activity period. During the high solar activity period, the prediction RRMSEs of both the Kriging and HAS methods decreased relative to the medium solar activity period, with the prediction results of the Kriging method decreasing by 15.80% and those of the HAS method decreasing by 8.13%. At low solar activity periods, the difference between the prediction RRMSEs of the Kriging method and the HAS method is 6.41%. Therefore, the prediction effects of both methods varied with the solar activity level, and the prediction RRMSEs became smaller when the solar activity improved in the middle solar activity period relative to the low solar activity period, while the prediction RRMSE became larger in the high solar activity period relative to the middle solar activity period. This shows the important influence of solar activity on the foF2 from this side.
2. The RRMSEs of the predictions using the two methods during the four seasons are given in Figure 8b. In spring, the HAS method predicted better results than the Kriging method, with a difference of 10.83% in the RRMSEs. In summer, the Kriging and HAS methods achieved the worst predictions. In autumn, the Kriging method reached the best prediction, but the prediction was still poor compared with that of the HAS method. In winter, the HAS method predicted the best results, with an RRMSE of 8.09%. Overall, the HAS method predicted better results than the Kriging method under all four seasons.
3. The RRMSEs of both methods during the day and at night are shown in Figure 8c. The prediction RRMSE of the Kriging method decreased by 7.66% during the daytime compared with nighttime, and the prediction RRMSE of the HAS method increased by 1.94% during the nighttime compared with daytime. Overall, the HAS method's predictions were better than the Kriging method both during the day and at night, and both method's predictions were better during the day.
4. Overall, the HAS method outperformed the Kriging method in different seasons, solar activity levels, and at daytime and nighttime. This confirms the effectiveness and precision of the HAS method introduced in this paper and provides a new approach and methodology for the prediction of ionospheric parameters.

To present the reconstruction outcomes of both methods in a more intuitive manner, Figure 9 shows the results of spatial reconstruction using the HAS method and the Kriging method at different times:

1. The reconstruction outcomes of the HAS and Kriging methods at 12:00 p.m. local time for the high solar activity year in November 2014 are illustrated in Figure 9a,b, respectively. The figures show that the value domains reconstructed by the HAS method ranged from 7.5 to 12, and the value domains reconstructed by the Kriging method ranged from 7.5 to 11.5, indicating that the values reconstructed by the HAS method would be larger than those reconstructed by the Kriging method in some regions. In addition, the results of the reconstruction by the HAS method can be observed as multiple obvious contour circles, which represent the large value variations of the local regions, with obvious high-value areas. In contrast, the contour lines in the reconstructed results of the Kriging method are relatively smooth, and there is no obvious local variation in the HAS method.
2. Figure 9e,f shows the distribution of the RRMSEs of the HAS and Kriging methods in predicting the seven stations at 12:00 p.m. local time for the high solar activity year in November 2014, respectively, and the RRMSE plots of the HAS method show that the RRMSEs were larger at some points in the plots but smaller at most stations. Compared with the prediction of the RRMSEs for the Kriging method, the HAS method predicted the RRMSEs of all seven stations better than the Kriging method.
3. The reconstruction outcomes of the HAS and Kriging methods at 12:00 a.m. local time for the low solar activity year in July 2018 are illustrated in Figure 9c,d, respectively.

The figure shows that the local area reconstructed by the HAS method had a large change in value. For example, an obvious high-value area can be seen in the upper right of the figure. The transition between the high-value and low-value areas in the reconstructed results of the Kriging method is relatively smooth, and the characteristics of the spatial distribution are not as obvious as those of the HAS method, which lacks some details.

4. Figure 9g,h shows the RRMSE distributions of the seven stations predicted by the HAS and Kriging methods, respectively, at 12:00 a.m. local time for the low solar activity year in July 2018. The RRMSE plots of the HAS method show that it was larger at the Perth station. All the other stations had smaller values than the predicted RRMSEs of the Kriging method, and as a whole, the HAS method was better. Overall, the HAS method is suitable for applications which are sensitive to local variations. However, it is important to note that some regions may have large RRMSEs.
5. Overall, the HAS method showed high accuracy and reliability in the spatial reconstruction of the foF2 at different times and locations. Compared with the Kriging interpolation method, the HAS method can more accurately capture the spatial variation characteristics of the ionospheric parameters with smaller prediction RRMSEs.

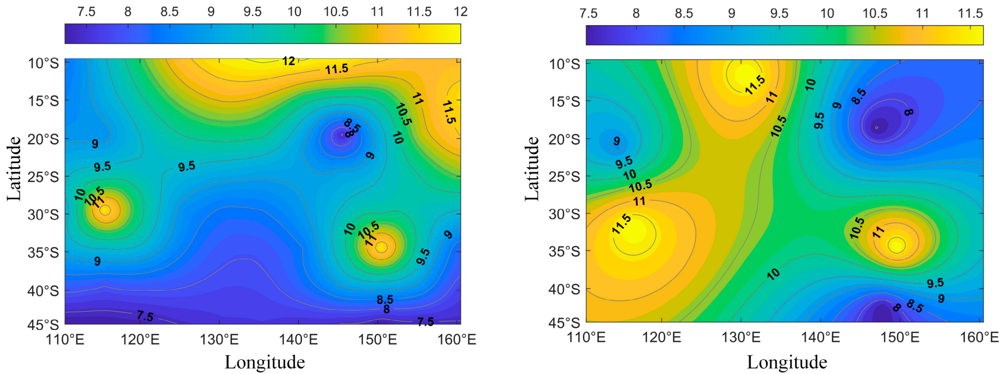

(a)HAS Brisbane 2014 Nov. 12:00 (b)Kriging Brisbane 2014 Nov. 12:00

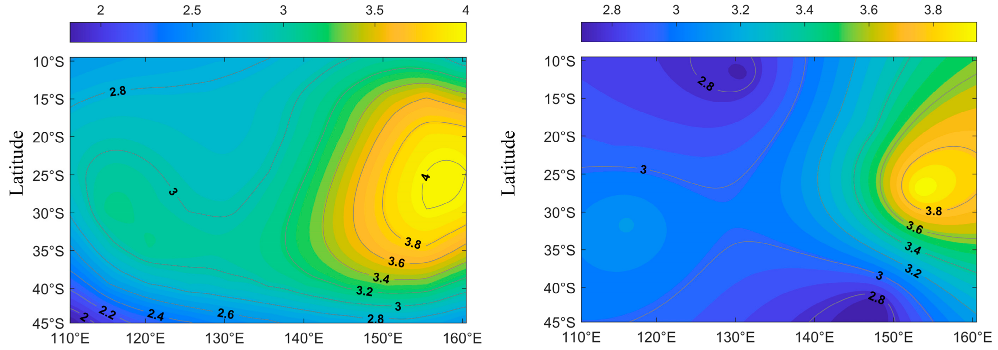

(c)HAS Canberra 2018 Jul. 0:00 (d)Kriging Canberra 2018 Jul. 0:00

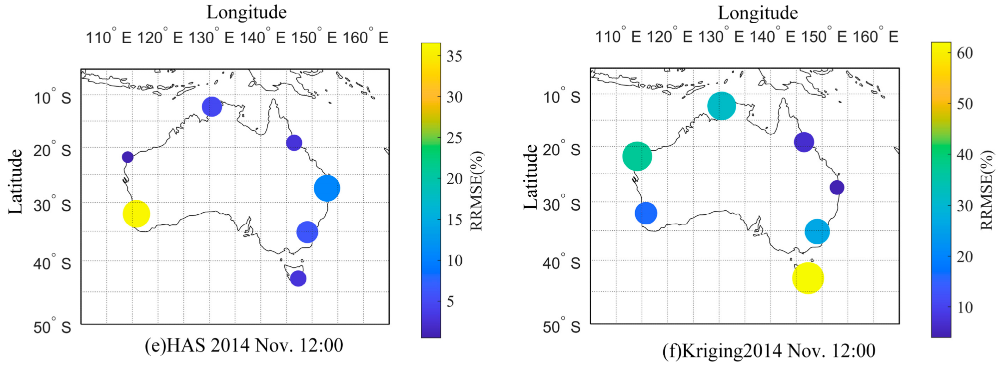

(e)HAS 2014 Nov. 12:00 (f)Kriging2014 Nov. 12:00

Figure 9. *Cont.*

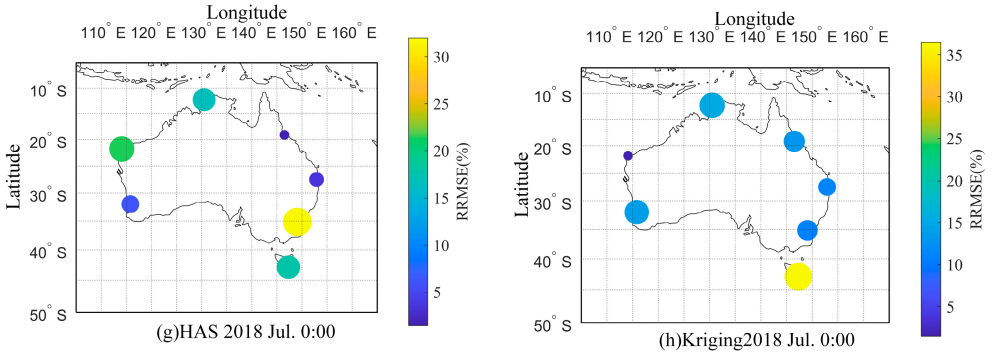

(g)HAS 2018 Jul. 0:00 (h)Kriging2018 Jul. 0:00

Figure 9. Comparison of reconstruction results. (**a**) The reconstruction outcomes of the HAS method at 12:00 p.m. local time for the high solar activity high in November 2014. (**b**) The reconstruction outcomes of the Kriging method at 12:00 p.m. local time for the high solar activity year in November 2014. (**c**) The reconstruction outcomes of the HAS method at 12:00 a.m. local time for the high solar activity year in July 2018. (**d**) The reconstruction outcomes of the Kriging method at 12:00 a.m. local time for the high solar activity year in July 2018. (**e**) Distribution of the RRMSEs of the HAS method in predicting the seven stations at 12:00 p.m. local time for the high solar activity year in November 2014. (**f**) Distribution of the RRMSEs of the Kriging method in predicting the seven stations at 12:00 p.m. local time for the high solar activity year in November 2014. (**g**) Distribution of the RRMSEs of the HAS method in predicting the seven stations at 12:00 a.m. local time for the low solar activity year in July 2018. (**h**) Distribution of the RRMSEs of the HAS method in predicting the seven stations at 12:00 a.m. local time for the low solar activity year in July 2018.

5. Conclusions

In this study, we introduced a novel technique named the HAS method for spatial reconstruction of the foF2 region. The foF2 ionospheric parameter of seven ionospheric stations in Oceania was reconstructed in sequence under different solar activity epochs, seasons, and local times, and the foF2 predicted data were compared with the actual data to verify the validity of the HAS method. Moreover, the prediction accuracy of the HAS model was compared with the IRI prediction model and Kriging interpolation method, and it was verified that the HAS method improved the accuracy. The validation results indicate that during different solar activity periods, the HAS method predicted the foF2 with a smaller RRMSE of 7.74% during moderate solar activity periods, which represented an improvement of 7.41% in prediction accuracy compared with the Kriging interpolation method. Across the four seasons, the HAS method predicted the foF2 with a smaller RRMSE of 8.09% in winter, showing a prediction accuracy which aligned closely with the actual observations from ionospheric stations, which had an RRMSE of 10.20%. The HAS method's prediction accuracy improved by 12.00% compared with that of the Kriging method. At different times, the HAS method predicted the foF2 with a smaller RRMSE of 9.23% during moderate solar activity periods, representing a 5.92% improvement in prediction accuracy compared with that of the Kriging interpolation method. The average RRMSE of the IRI prediction model under the validation dataset was 12.35%, and the prediction accuracy of the HAS method improved by 2.06% compared with that of the IRI prediction model. These results demonstrate the correctness and effectiveness of the proposed HAS method.

Author Contributions: Conceptualization, J.W. and H.H.; methodology, J.W. and H.H.; software, J.W., H.H. and Y.S.; validation, J.W. and H.H.; formal analysis, J.W., H.H. and Y.S.; investigation, J.W., H.H. and Y.S.; resources, J.W.; data curation, J.W., H.H. and. Y.S.; writing—original draft preparation, J.W. and H.H.; writing—review and editing, J.W. and Y.S.; visualization, J.W. and H.H.; supervision, J.W., H.H. and Y.S.; project administration, J.W.; funding acquisition, J.W. All authors have read and agreed to the published version of the manuscript.

Funding: This research was funded by the National Natural Science Foundation of China under grant no. 62031008 and the State Key Laboratory of Complex Electromagnetic Environment Effects on Electronics and Information Systems under grant no. CEMEE2022G0201.

Data Availability Statement: No new data were created or analyzed in this study. Data sharing is not applicable to this article.

Conflicts of Interest: The authors declare no conflicts of interest.

References

1. Bilitza, D.; Pezzopane, M.; Truhlik, V.; Altadill, D.; Reinisch, B.W.; Pignalberi, A. The International Reference Ionosphere model: A review and description of an ionospheric benchmark. *Rev. Geophy.* **2022**, *60*, e2022RG000792. [CrossRef]
2. Zhou, W.Q.; Yu, Y.; Wan, W.X.; Liu, L.B. Tidal variations of the ionospheric foF2 in mid-latitude ionosphere. *Chin. J. Geophys.* **2018**, *61*, 30–42. [CrossRef]
3. Zhen, W.M.; Ou, M.; Zhu, Q.L.; Dong, X.; Liu, D. Review on ionospheric sounding and modeling. *Chin. J. Radio Sci.* **2023**, *38*, 625–645. [CrossRef]
4. Wang, J.; Yang, C.; An, W.X. Regional refined long-term predictions method of usable frequency for HF communication based on machine learning over Asia. *IEEE Trans. Antennas Propag.* **2022**, *70*, 4040–4055. [CrossRef]
5. Laštovička, J. Long-Term Changes in Ionospheric Climate in Terms of foF2. *Atmosphere* **2022**, *13*, 110. [CrossRef]
6. Wang, J.; Shi, Y.F.; Yang, C.; Zhang, Z.G.; Zhao, L. A short-term forecast method of maximum usable frequency for HF communication. *IEEE Trans. Antennas Propag.* **2023**, *71*, 5189–5198. [CrossRef]
7. Wang, J.; Han, H.; Shi, Y.F.; Yang, C.; Liu, Y.R.; Wang, Z.Q. Comparison and validation of MOF observations and MUF predictions from seven different models. *Adv. Space Res.* **2024**, *74*, 2452–2462. [CrossRef]
8. Che, L.; Ou, M.; Chen, Q.D.; Cai, H.T.; Zhen, W.M.; Chen, L.J.; Jin, R.M. An optional algorithm for ionosphere TEC region reconstruction. *Chin. J. Radio Sci.* **2022**, *37*, 875–882. [CrossRef]
9. Shi, Y.F.; Yang, C.; Wang, J.; Zhang, Z.G.; Meng, F.Y.; Bai, H.M. A forecasting model of ionospheric foF2 using the LSTM network based on ICEEMDAN decomposition. *IEEE Trans. Geosci. Remote Sens.* **2023**, *61*, 4108416. [CrossRef]
10. Liu, Y.R.; Yu, Q.; Shi, Y.F.; Yang, C.; Wang, J. A Reconstruction Method for Ionospheric foF2 Spatial Mapping over Australia. *Atmosphere* **2023**, *14*, 1399. [CrossRef]
11. Pradipta, R.; Valladares, C.E.; Carter, B.A.; Doherty, P.H. Interhemispheric propagation and interactions of auroral traveling ionospheric disturbances near the equator. *J. Geophys. Res. Space* **2016**, *121*, 2462–2474. [CrossRef]
12. Sandwell, D.T. Biharmonic spline interpolation of GEOS-3 and SEASAT altimeter data. *Geophys. Res. Lett.* **1987**, *14*, 139–142. [CrossRef]
13. Jones, W.B.; Gallet, R.M. Representation of diurnal and geographic variations of ionospheric data by numerical methods. *J. Res. Natl. Bur. Stand.* **1962**, *29*, 129–147. [CrossRef]
14. Chen, L.J.; Zhen, W.M.; Ou, M.; Yu, X.; Song, F.L. A method of ionospheric foF2 reconstruction in low and middle latitudes of the world based on stepwise linear optimal estimation. *Chin. J. Radio Sci.* **2021**, *36*, 36–42.
15. Huang, L.; Zhang, H.P.; Xu, P.L.; Geng, J.H.; Wang, C.; Liu, J.N. Kriging with Unknown Variance Components for Regional Ionospheric Reconstruction. *Sensors* **2017**, *17*, 468. [CrossRef] [PubMed]
16. Bilitza, D.; Altadill, D.; Truhlik, V.; Shubin, V.; Galkin, I.; Reinisch, B.; Huang, X. International Reference Ionosphere 2016: From ionospheric climate to real-time weather predictions. *Space Weather* **2017**, *15*, 418–429. [CrossRef]
17. ITU-R Recommendations. ITU-R Reference Ionospheric Characteristics. 2012, 1239-3. Available online: https://www.itu.int/rec/R-REC-P.1239-3-201202-S/en (accessed on 1 July 2024).
18. Xiong, P.; Zhai, D.L.; Long, C.; Zhou, H.Y.; Zhang, X.M.; Shen, X.H. Long short-term memory neural network for ionospheric total electron content forecasting over China. *Space Weather* **2021**, *19*, e2020SW002706. [CrossRef]
19. Wang, J.; Liu, Y.R.; Shi, Y.F. A High Accuracy Spatial Reconstruction Method Based on Surface Theory for Regional Ionospheric TEC Prediction. *Space Weather* **2023**, *21*, e2023SW003663. [CrossRef]
20. Yue, T.X.; Wu, C.C.; Liu, Y.; Du, Z.P.; Zhao, N.; Jiao, Y.M.; Xu, Z.; Shi, W.J. HASM quantum machine learning. *Sci. China Earth Sci.* **2023**, *66*, 1937–1945. [CrossRef]
21. Yue, T.-X.; Zhang, L.-L.; Zhao, N.; Zhao, M.-W.; Chen, C.-F.; Du, Z.-P.; Song, D.-J.; Fan, Z.-M.; Shi, W.-J.; Wang, S.-H.; et al. A review of recent developments in HASM. *Environ. Earth Sci.* **2015**, *74*, 6541–6549. [CrossRef]
22. Wang, J.; Zhao, M.-W.; Jiang, L.; Yang, C.-C.; Huang, X.-L.; Xu, Y.; Lu, J. A new strategy combined HASM and classical interpolation methods for DEM construction in areas without sufficient terrain data. *J. Mt. Sci.* **2021**, *18*, 2761–2775. [CrossRef]
23. Liu, Y.; Wu, B.W.; Yue, T.X. Spatiotemporal analysis of global atmospheric XCO2 concentrations before and after COVID-19 using HASM data fusion method. *Front. Environ. Sci.* **2023**, *10*, 1079480. [CrossRef]
24. Global Ionosphere Radio Observatory. Available online: https://giro.uml.edu/index.html (accessed on 1 July 2024).
25. Yue, T.X. *Surface Modeling: High Accuracy and High Speed Methods*; CRC Press: Boca Raton, FL, USA, 2011.
26. Jiang, L.; Zhao, M.; Yue, T.; Zhao, N.; Wang, C.; Sun, J. A modified HASM algorithm and its application in DEM construction. *Earth Sci. Inform.* **2018**, *11*, 423–431. [CrossRef]

27. Zhao, N.; Yue, T.X. A modification of HASM for interpolating precipitation in China. *Theor. Appl. Climatol.* **2014**, *116*, 273–285. [CrossRef]
28. Chen, C.F.; Yue, T.X.; Li, Y.Y. A high speed method of SMTS. *Comput. Geosci.* **2012**, *41*, 64–71. [CrossRef]
29. Chen, C.; Yue, T.X.; Dai, H.L.; Tian, M.Y. The smoothness of HASM. *Int. J. Geogr. Inf. Sci.* **2013**, *27*, 1651–1667. [CrossRef]
30. ISES Solar Cycle Sunspot Number Progression. Available online: https://www.swpc.noaa.gov/products/solar-cycle-progression (accessed on 17 July 2023).
31. Wang, S.K.; Jiao, P.N.; Liu, W. Improved Kriging technique of ionospheric parameter foF2 instantaneous mapping. *Chin. J. Radio Sci.* **2006**, *21*, 166–171.